Carbon Dioxide Capture by Niobium Polyoxometalate Fragments

Zhiwei Mao,[1] Mokhtar Rashwan,[2] Eduard Garrido-Ribo,[1] Makenzie Nord,[1] Lev N. Zakharov,[1] T. Wesley Surta,[1] Ahmet Uysal,[2]*May Nyman[1]*

[1]Department of Chemistry, Oregon State University, Corvallis OR 97331 USA.

[2]Chemical Sciences and Engineering Division, Argonne National Laboratory, Lemont, Illinois 60439, USA

ABSTRACT: High oxidation state metal cations have diverse roles in carbon dioxide removal (direct air capture and at-the-source) including providing basic oxygens for chemisorption reactions, direct binding of carbonate, and low-temperature release of CO_2 for regeneration of capture media. Moreover, metal oxide systems and aqueous metal-oxo species are stable in harsh conditions. Here we demonstrate the carbon capture ability of niobium polyoxometalates (POMs) as aqueous solutions, specifically $[Nb_6O_{19}]^{8-}$, Nb_6. Upon exposure of Nb_6 solutions to CO_2, Nb_6 fragments and binds carbonate, evidenced by crystallization of Nb-carbonate POMs including $[Nb_{22}O_{53}(CO_3)_{16}]^{28-}$and $[Nb_{10}O_{25}(CO_3)_6]^{12-}$. While Rb/Cs^+ counter cations yielded crystal structures to understand the chemisorption processes, K^+ counter cations enabled higher capture efficiency (based on CO_3:Nb ratio), as determined by CHN analysis and thermogravimetry-mass spectrometry of the isolated solids. Sum frequency generation (SFG) spectroscopy also showed higher carbon capture efficiency of the K-Nb_6 solutions at the air-water interface, while small-angle X-ray scattering (SAXS) provided insight into the role of the alkalis in influencing these processes. Tetramethylammonium counter cations (TMA), like K^+, demonstrated high efficiency of carbonate chemisorption at the interface, but SAXS and Raman of the bulk showed a predominance of a Nb_{24}-POM ($H_xNb_{24}O_{72}$, x~9) that can bind carbonate only minimally, and any carbonate present is likely free bicarbonate instead of Nb-bound. Control experiments show that all carbonate present at the interface is Nb-bound, and the Nb-carbonate species are stabilized by alkalis, demonstrating a synergistic role of alkalis and high oxidation state metal cations in chemisorption of CO_2. Of fundamental importance, this study presents rare examples of directing POM speciation with a gas, instead of liquid phase acid or base.

INTRODUCTION

Amongst the most crucial chemical reactions are those involving removal of carbon dioxide from air. Understanding and exploiting this reaction under a variety of conditions is important to mitigate climate change. According to the Paris Climate Accords; we must limit global warming to 1.5 °C by 2100; and greenhouse gases, including CO_2, must decline by an ambitious 43% by 2030. Both removal of legacy CO_2 (direct air capture, DAC) and point source capture are important to reach these goals. Metal oxide-based systems[1] include basic solids such as zeolites,[2] alkali/alkaline earth oxides/hydroxides,[3-6] amine-functionalized oxides,[7] layered double hydroxides,[8-10] and minerals such as clays[11] and olivine (Mg_2SiO_4).[12] The reactivity of all of these basic oxides is ultimately attributed to the amine, alkali or alkaline earth component, while the role of heterometals (i.e. Si, Al and dopants/impurities such as Fe) that are also present and important, is less-well understood.

Considering chemisorption by basic metal oxides in which a CO_2 molecule is captured via formation of CO_3^{2-} or HCO_3^-, there is a conundrum between the energetics of sorption and release (for regeneration). For example, the reaction of CO_2 with alkali and alkaline earth hydroxides is strongly exothermic (favored), but regeneration temperature (decomposition temperature) is extremely high; i.e. ~900 °C, for $CaCO_3$ and ~1200 °C for K_2CO_3.[13] On the other hand, recent studies have shown that the addition of higher valence metal oxides including titanates, V_2O_5, MoO_3, WO_3, and ZrO_2, can catalyze the release of CO_2 from amine-based CO_2-sorbents; and for example, decrease the regeneration temperature of monoethanolamine (MEA, the industrial standard for point-source CO_2 capture).[14-16] In addition, the orthovanadate ion increases CO_2 capture rate in aqueous media, attributed to the ability of VO_4^{3-} to deprotonate water and accelerate hydration of CO_2.[17] We recently demonstrated the release temperature of captured CO_2 decreases from >800 °C to 500 °C from physical mixtures of alkali carbonate and vanadate, compared to the alkali carbonate alone.[18] Meanwhile, release of air-captured carbonate directly bound to V^{5+} in a molecular form is accomplished at 250 °C,[18] demonstrating the direct role of the metal in both CO_2 capture and release.

The potential roles of high oxidation state metals in both carbon capture and release/regeneration warrants more indepth investigation to: 1) diversify and enhance carbon capture materials and chemistry, 2) delineate roles of alkali/alkaline earth metals and higher oxidation state metals in carbon capture for complex metal oxide systems, and 3) understand the role of metal charge in CO_2 capture/release. Building on our recent studies of peroxovanadates,[18] we hypothesize that additional highly-charged metal cations in aqueous environments can catalyze hydration of CO_2, directly bind the formed carbonate by coordination sphere expansion, and catalyze lower temperature release, due to the highly oxophilic nature of such metals.

Polyoxometalates (POMs) are anionic, polynuclear metal-oxo clusters that are composed of some of the same d^0-transition metals as the aforementioned oxoanion or metal oxide catalysts for CO_2 release from carbon capture systems (V^{5+}, Nb^{5+}, Ta^{5+}, Mo^{6+}, W^{6+}). They offer multiple attractive characteristics of carbon capture, release, and conversion. For capture, these metals can robustly form up to seven bonds (including to carbonate), and they usually possess alkali countercations. These oxophilic metals can polarize the C-O bond and promote low temperature release, as demonstrated in aforementioned studies.[14-17] Finally, some of these metals, especially in the POM form, possess reversible redox activity (V, Mo, W), which may assist in conversion, if desired. Regardless of the speciation, niobium POMs have the added benefit of highly basic oxygens for carbon capture, in particular the Lindqvist ion, $[Nb_6O_{19}]^{8-}$, (**Nb_6**, a superoctahedron of six mutually edge-sharing

NbO_6-octahedra, **figure 1**).[19-20] **Nb_6** has a concentration-dependent, self-buffering pH and stability range of 12-14 via protonation of bridging oxo ligands and corresponding release of hydroxide in aqueous environments, i.e.;

$$[Nb_6O_{19}]^{8-} + H_2O \rightarrow [Nb_6O_{19-x}(OH)_x]^{(8-x)-} + xOH^- \quad (1)$$

where x=1-3. Prior studies demonstrated Nb-POMs with coordinated carbonate are accessible by adding carbonate to solution,[21-22] or from adventitious carbonate impurities in the alkaline solution.[23]

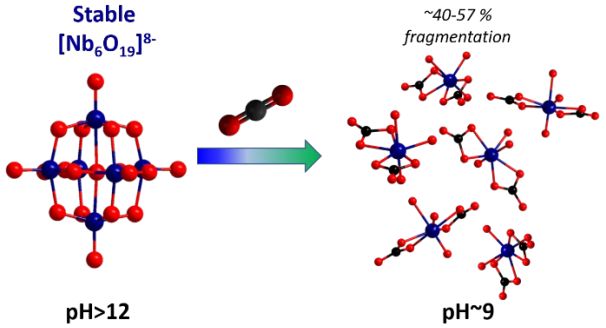

Figure 1. Schematic illustrating the process of Nb_6 (left) disassembly in solution driven by CO_2 infusion as demonstrated in this study, with stabilization of monomers via carbonate ligation. Niobium is blue, oxygen is red.

In this study, we hypothesized that Nb-POM speciation change and concomitant gaseous CO_2 capture via Nb-carbonate binding could be achieved, using aqueous solutions of **Nb_6**. Up-to-date computed speciation diagrams[24] predict that decreasing the pH of an **Nb_6** solution (i.e. from 14 to ~9) would drive topology and nuclearity from **Nb_6** to **Nb_7** ($[Nb_7O_{20}(OH, H_2O)_2]^{(5-7)-}$). On the other hand, experiments and computation demonstrated speciation change from **Nb_{10}** ($[Nb_{10}O_{28}]^{6-}$) to **Nb_7** can be promoted by pH increase from ~7 to ~9, via cleaving an **Nb_3** fragment.[25-26] Those studies complete the Nb-speciation diagram across the pH range that Nb-oxo species are sufficiently soluble in water (pH 7 - 14)[27] without using chelating ligands (i.e. oxalate[28]). Because **Nb_7** is **Nb_6** decorated with one additional monomer, the predicted change from **Nb_6** to **Nb_7** cannot happen without disassembly of **Nb_6,** producing Nb-monomers, where monomers never been experimentally observed or isolated.

Via crystal structure of $[Nb_{22}O_{53}(CO_3)_{16}]^{28-}$ (**$Nb_{22}CO_3$**) from up to 2M solutions of **Nb_6** with Rb^+ or Cs^+ counter cations, we demonstrate that ~50% of the Nb_6 units fragment into monomers via CO_2 infusion, and the monomers bind two carbonate ligands per Nb (**figure 1**). With K^+ counterions, gels instead of crystalline product is obtained, and the CO_2 capture capacity (by weight % carbon) nearly doubles. Characterization of the solutions (via small angle X-ray scattering, SAXS) and gels (by X-ray total scattering) suggests the gel contains networks of carbonate-ligated Nb building-units observed in **$Nb_{22}CO_3$**. SAXS of the CO_2-infused alkai-Nb_6 solutions suggest less direct contact ion-pairing of K^+ with Nb_6 enables more extensive fragmentation and carbonate binding, compared to the Rb/Cs^+ analogues. Sum frequency generation spectroscopy (SFG) also shows higher levels of bound CO_3^{3-} at the interface, for K-Nb_6 solutions compared to the Rb/Cs-Nb_6 solutions. This indicates the alkali-Nb_6 ion-pair formation at the interface directly impacts CO_2 chemisorption by Nb-carbonate bonding. Although TMA-Nb_6 (TMA=tetramethylammonium) is highly soluble and produces alkaline solutions, similar to the K/Rb/Cs^+ counterparts, SFG suggests different behavior. Nb-carbonate bonding is abundant at the interface, but only minimally so in the bulk, as described by multiple solution characterization techniques. In sum, these studies confirm the niobyl ($Nb{=}O^{3+}$) directs CO_2 chemisorption, while the different cations (alkalis) plays various supporting roles. These include stabilizing Nb-carbonate species in solution and solids, and tuning reactivity based on ion-pairing in bulk and at the interface. Finally, while most POM and other oxocluster speciation reactions are driven with addition of acid or base in solution to promote olation and oxolation reactions, this is the first demonstration to our knowledge, where a gas can drive POM formation reactions.

RESULTS AND DISCUSSION

Exposure of high concentration solutions of both Rb-**Nb_6** and Cs-**Nb_6** to a CO_2 rich environment (details summarized in **Table S1**) resulted in crystallization of **$Nb_{22}CO_3$**, and/or **$Nb_{10}CO_3$**. We report three complete structures, Rb and Cs salts of **$Nb_{10}CO_3$** and Rb salt of **$Nb_{22}CO_3$**. We also identified the POM plus key Cs positions for the Cs salt of **$Nb_{22}CO_3$**, but the X-ray data is not publishable. The three complete structures are all summarized in **Table S2**. The Cs-**$Nb_{22}CO_3$** structure exhibited considerable disorder in the Cs/H_2O lattice species, and many NPD atoms when attempting to perform anisotropic refinement. These issues could not be satisfactorily resolved, and repeated attempts to obtain quality crystals of Cs-**$Nb_{22}CO_3$** yielded Cs-**$Nb_{10}CO_3$**, but the two structures are closely related. Therefore, the structure of Cs-**$Nb_{22}CO_3$** will be discussed only in comparison to Rb-**$Nb_{22}CO_3$**, and to model bulk or solution phase data.

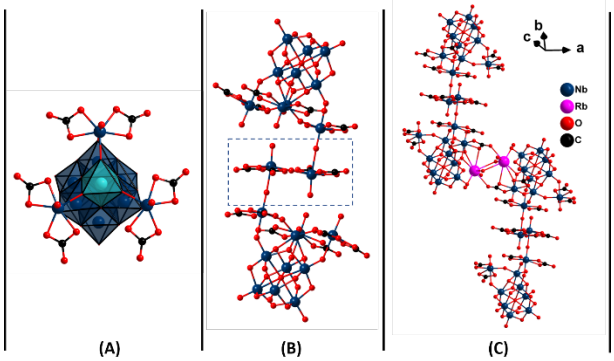

Figure 2. Views of **$NbCO_3$** POMs. A) The $Nb_{10}CO_3$ (and subunit of **$Nb_{22}CO_3$**). The dark blue polyhedra make up the Nb_6 core, while the addenda polyhedron in the Nb_7 unit is highlighted in light blue. The three $NbO(CO_3)_2^+$ are shown in ball-and-stick representation. Nb is dark blue spheres, C is black, and oxygen is red. B) The complete **$Nb_{22}CO_3$** cluster shown in ball-and-stick representation. C) Dimerization of **$Nb_{22}CO_3$** via the Rb^+-counterions (pink spheres) in the crystalline lattice of **Rb-$Nb_{22}CO_3$** (identical linkage is shown for **Cs-$Nb_{22}CO_3$**).

The anion that is formulated $[Nb_{22}O_{53}(CO_3)_{16}]^{28-}$ (**figure 2b**) is essentially a dimer of two **$Nb_{10}CO_3$** units reported prior from the reaction of decaniobate, $[Nb_{10}O_{28}]^{6-}$ (**Nb_{10}**) with potassium carbonate.[21] The two **$Nb_{10}CO_3$** units are linked by Nb-dimer $[NbO(CO_3)_2]_2O$ (**figure 2b**, inside the dashed box), and the only symmetry element of **$Nb_{22}CO_3$** is an inversion center, translating the two Nb_{11} halves. Briefly, **$Nb_{10}CO_3$** is composed of an Nb_7-cluster, where the 7th addenda polyhedron with three terminal oxos bridges to three $NbO(CO_3)_2$ polyhedra (**figure 2a**). Each of these $NbO(CO_3)_2$ polyhedra bridge to a second $Nb{=}O_{yl}$ of the core **Nb_6**. The seven core Nb are in a distorted octahedral coordination environment. The $Nb{=}O_{yl}$ terminal oxos exhibit somewhat longer than expected bond lengths, ~1.77 Å on average (**see Table S3,** these are ~0.05 Å longer than typically observed for Nb-POMs). The μ_2-oxos of the Nb_7 core range from ~1.89 – 2.05 Å. The eight

$NbO_3(CO_3)_2$ polyhedra within **$Nb_{22}CO_3$** exhibit distorted pentagonal bipyramidal coordination with two chelating carbonate ligands in the equatorial plane. These Nb-$O_{carbonate}$ bond distances are ~2.1

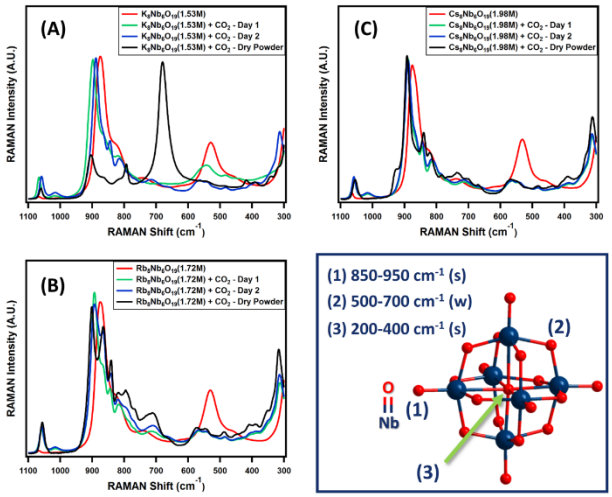

Figure 3. Raman spectra tracking the species evolution with CO_2 infusion for K-Nb_6 (**A**), Rb-Nb_6 (**B**) and Cs-Nb_6 (**C**). The curves are scaled so that the highest intensity peak is roughly equivalent, for ease of comparison. (**D**) Illustration of Nb_6 and the Nb-O Raman vibrational frequency correlation of the different oxo-ligands.

Å, and the fifth bond in the equatorial plane is an oxo that bridges to a neighboring Nb; either another $NbO_3(CO_3)_2$, or a Nb within the Nb_7 unit. In the axial direction perpendicular to the pentagonal plane, there is a short Nb=O_{yl} bond (~1.77 Å) trans to a long Nb-O bond (~2.22 Å), typical of POM topologies.

For both Rb-**$Nb_{22}CO_3$** and (tentative) Cs-**$Nb_{22}CO_3$**, polyanions are linked by alkalis in a linear fashion (**figure S1a**), leading to the elongated crystal morphology (**figure S2b, S2c**). Rb/Cs^+ in dimer pairs bond to both carbonate ligands and μ_2O-Nb_2 oxygens (Rb-O ~2.9-3.0 Å). The alkalis dimerize by bridging water molecules (**figure 2c** for the Rb-analogue). A total of 28 Rb counterions were located in the lattice per **$Nb_{22}CO_3$** unit in both fully and partially occupied positions, charge-balancing the POM with a moiety formula of $Rb_{28}[Nb_{22}O_{53}(CO_3)_{16}]\cdot 54H_2O$.

Crystals of **$Nb_{10}CO_3$** with both Rb^+ and Cs^+-counterions were also structurally characterized, mixed with **$Nb_{22}CO_3$** crystals. However, quantification of carbonate for both the Rb and Cs POMs is more consistent with **$Nb_{22}CO_3$**, discussed later. All counterions were also found for these structures, with moiety formulae of $Rb_{12}[Nb_{10}O_{25}(CO_3)_6]\cdot 12H_2O$ and $Cs_{12}[Nb_{10}O_{25}(CO_3)_6]\cdot 15H_2O$, respectively (**Table S2**). Rb-**$Nb_{10}CO_3$** (monoclinic, $P2_1/n$) and Cs-**$Nb_{10}CO_3$** (monoclinic, $C2/c$) are essentially identical in their lattice arrangement of POMs and alkalis. Both exhibit a double-row, or ladder-like arrangement of the POMs along the *b*-axis, connected along the rows and between the rows by alkalis (**figure S2**). Essentially one alkali links between two **$Nb_{10}CO_3$** units in both directions, bonding both the POM and the carbonate oxygens. Each alkali bonds between one and three carbonate ligands, reinforcing their importance in stabilizing the **$Nb_{10}CO_3$** unit that does not form when TMA counterions are present instead.

Raman spectra of ~2 M K-**Nb_6**, Rb-**Nb_6** and Cs-**Nb_6** solutions are shown in **figure 3** upon dissolution (red spectra) and exposure to an enhanced CO_2 environment to accelerate spectral measurements (see SI for details). We have made general peak assignments based on those known for Nb_6 and other Nb oxide phases, reported prior.[29-31] (**figure 3d, Table S3, figure S3**). In general, longer bonds correspond with lower frequency vibrations (cm^{-1}). For each of these solutions, there are two main peaks observed; between 500-600 cm^{-1}, which corresponds with μ_2-ONb_2 (bridging oxos), and the peak between 850-950 cm^{-1} corresponds with the Nb=O units. At the limit of the data collection range, the peak between 300-400 cm^{-1} corresponds with the central μ_6-ONb_6. Interestingly, with CO_2 infusion for two days, single broad peaks evolve to multiple peaks (specifically for μ_2-ONb_2 and Nb=O vibrations), covering a wider frequency range. This can be explained by the wider range of Nb-O bond distances in the **$Nb_{10}CO_3$** and **$Nb_{22}CO_3$** structures that dominate these solutions and precipitated solids, compared to in Nb_6 (see histograms, **figures S4-S6**). The isolated dry powders (Rb/Cs^+ analogues) show similar peak positions that become narrower and sharper, attributed to the lack of H-bonding from the aqueous environment.

Raman of the solid obtained from CO_2 infusion of K-Nb_6 (**figure 3a**) is quite different than the Rb/Cs^+ analogues, as is the solution. The solid phase has two distinct peaks in the Nb=O range, but much diminished compared to the highest intensity peak at 680 cm^{-1}. This is a unique feature, not present in any other spectrum collected in this study. The peak is not attributed to niobium oxide (our first hypothesis, **Table S3**). According to a prior survey and summary of Nb-O bond distances and their observed Raman stretches, we estimate that the gel-precipitate obtained from CO_2 infusion of K-Nb_6 has a predominance of Nb-O bond lengths around 1.85-1.9 Å. Both the higher CO_2 capture capacity of the K-Nb_6 solutions and the considerably more economical composition inspired us to further investigate the solution and solid-state structure of this CO_2 capture system, discussed below along with the CO_2 quantification results.

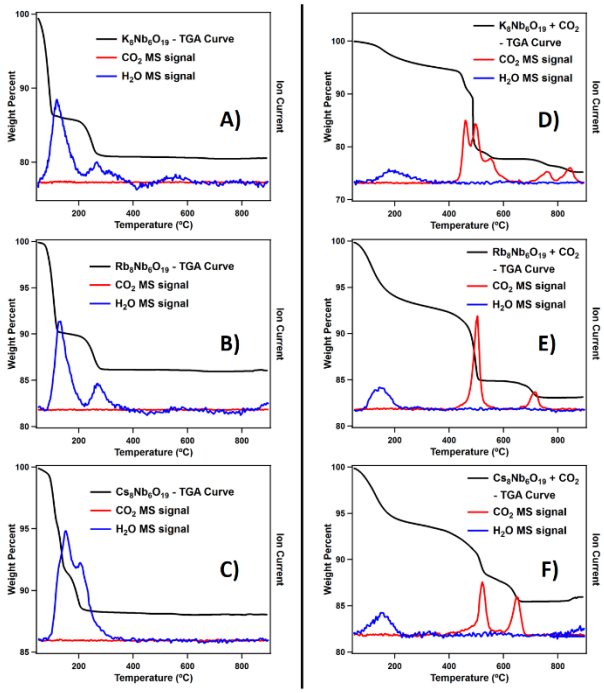

Figure 4. TGA-MS spectra illustrating the release temperatures of captured CO_2, K-Nb_6 (**A**), Rb-Nb_6 (**B**), Cs-Nb_6 (**C**), K-Nb_6 plus CO_2 (**D**), Rb-Nb_6 plus CO_2 (**E**), Cs-Nb_6 plus CO_2 (**F**). See **Table S4** for quantification of each weight loss event.

Thermogravimetric analysis with tandem mass spectrometry (TGA-MS, **figure 4**) provides both weight % CO_2 (combined with CHN analysis, **Table 1**) captured for each Nb_6 solution, as well as the temperature of release. For all three solutions, there is good agreement between CHN and TGA-MS quantification. Translated to ratio of CO_2:Nb, this is also in agreement with the crystal struc-

tures of **$Nb_{22}CO_3$**, indicating Nb-speciation of the precipitated solids are primarily Nb_{22} at the time of analysis. The K-Nb_6 exhibits a higher weight percent CO_2 than expected, suggesting further deconstruction of the Nb_6-units via carbonate bonding. This hypothesis was reinforced by PDF (pair distribution function) analysis from total X-ray scattering, discussed later.

Table 1. Quantification of captured CO_2

A^+-Nb_6 (~2M)[1]	Wt% CO_2 (C) from TGA-MS	Wt% C from CHN	CO_2: Nb ratio	CO_2:Nb ratio, Nb_{22} structure	% Nb_6 fragmented[2]
K	19.3 (5.3)	5.0	1.13	N/A	57%
Rb	10.0 (2.7)	2.8	0.73	0.73	37%
Cs	8.4 (2.3)	2.3	0.72		

[1]exact concentrations are K-Nb_6:1.53M, Rb-Nb_6:1.72M, Cs-Nb_6:1.98M (**Table S1**). Nb_6 clusters with different cations have different solubilities, and Nb_6 solution concentrations were optimized for best carbon capture performance.
[2]based on the 2:1 CO_3:NbO ratio of carbonate-ligated Nb in the reported structures.

Release of the niobium-bound carbonate occurs between 400-550 °C for regeneration, several hundred degrees lower than that associated with the any of the alkalis (K^+, Rb^+ or Cs^+, see **Tables S4-S5** for detailed analysis of TGA-MS data). The temperature of release is dependent on its coordination environment in the solid. Both the solids derived from the Rb-Nb_6 and Cs-Nb_6 solutions have a single CO_2 peak around 500 °C, attributed to the Nb-bound carbonate, wherein quantification of carbon capture is consistent with the majority of the solid containing Nb_{22}. Nb_{22} has two unique Nb-carbonate environments; that of the Nb_{10}-carbonate unit and the $[NbO(CO_3)_2]_2O$ bridge. However, all Nb=O chelate two carbonates and bridge to two addition Nb=O. Therefore, the carbonate coordinate environment is similar for these two sites, and it is reasonable that the release temperature is similar. Interestingly the solid derived from CO_2-infused K-Nb_6 has three release temperatures attributed to Nb-bound carbonate; at 460, 500 and 555 °C. This is consistent with the presence of multiple Nb-CO_3 coordination environments in this solid. In general, we expect binding of high oxidation state metals to polarize the C-O bond, enabling the release of the CO_2 at lower temperatures. For example, a carbonate chelating one Nb=O and bridging to a second Nb=O could exhibit a lower release temperature. Alternatively, protonation (i.e. $NbOCO_2H$) could also lower the release temperature. A less sterically hindered carbonate (i.e. octahedral Nb instead of pentagonal bipyramidal Nb) might release at a slightly higher temperature. By comparison, our prior reported $VO(O_2)_2(CO_3)^{3-}$ that forms via DAC as a solid simultaneously released peroxide and CO_2 at 240 °C,[32] likely due to the concerted simultaneous release of the adjacently-bound peroxide.

Small angle X-ray scattering (SAXS) provided insight into speciation change of Nb_6 with CO_2 infusion, prior to precipitation/crystallization (**figure 5**). With CO_2 infusion for all three alkali Nb_6 solutions, there is clearly an increase in scattering species size, noted by the order of magnitude increase in scattering intensity (I(q)) and the shift of the Guinier curves to lower-q. Increased polydispersity is also noted by the steepening slope at q<0.1 $Å^{-1}$. Redissolved crystals of Rb-**$Nb_{22}CO_3$** produced a scattering curve very similar to that of CO_2-infused Rb-Nb_6 and Cs-Nb_6 solutions, suggesting the species of these crude solutions (and obtained precipitates) are predominantly **$Nb_{22}CO_3$**, consistent with the quantification of captured carbon. As noted above, the Nb_{22} units link into chains via alkalis (Rb or Cs, **figure S1**), so we simulated scattering data of several chain lengths, and found the Nb_{22}-dimer (shown in **figure 2c**) provided the closest match. CO_2-infused K-Nb_6 solution scattering is notably different. The even greater steepening and shift of the Guinier elbow to lower-q suggests respectively greater polydispersity and larger aggregates compared to the Rb and Cs solutions. In the simulated **$Nb_{22}CO_3$** -dimer curve (**figure 5a**), there is a characteristic plateau feature around q=0.3-0.5 $Å^{-1}$. This is also observed in all the experimental scattering of CO_2-infused Nb_6 solutions including K-Nb_6, suggesting **$Nb_{22}CO_3$** is also present in these solutions, within the obtained precipitates and gels. Notably, simulation of scattering of longer linear **$Nb_{22}CO_3$**-polymers did not yield a satisfactory match to the CO_2-infused K-Nb_6 solution, suggesting other species are present.

Given the Nb-POM polydispersity in these solutions is largely driven by differentiating connectivity by the alkalis, we chose a simple size distribution analysis (maximum entropy method[33-34]) to approximate and compare sizes and size distribution (**figure 5b, S7**). The size distribution for all three CO_2-infused solutions exhibits a major peak with diameter of 19 Å (K), 22 Å (Rb), and 24 Å (Cs), consistent with the ~22 Å length and 20 Å width of Nb_{22} from the crystal structure (**figure S7**). The trend of slightly increasing size with increasing alkali radius is commensurate with inherent increased direct ion-pairing for the alkali series, as observed in prior SAXS studies of Nb_6 solutions.[35] The second peak observed for all three solutions (~35 Å) is also consistent with a dimension of Nb_{22}. Notably and consistent with the q-space scattering data, the CO_2-infused K-Nb_6 scattering exhibits larger dissolved aggregates and more polydispersity than the Rb and Cs analogues.

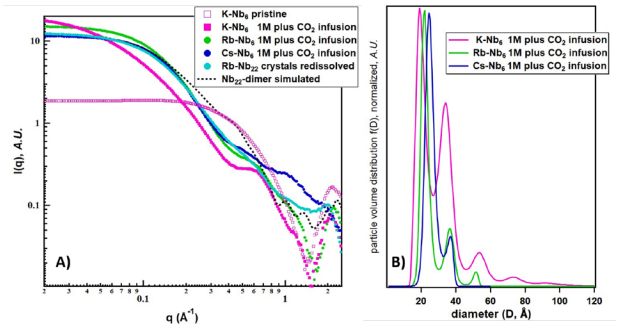

Figure 5. A) SAXS curves and B) size distribution analysis for CO_2-infused Nb_6 solution phase studies.

To further characterize the CO_2-infused Nb_6 solutions, particularly the K-analogue that has no distinct associated crystal structure, we used (benchtop) pair distribution function (PDF) from total X-ray scattering of solids collected from the three solutions (**figure 6, Table S6** shows the PDF, **figure S8** shows the unprocessed scattering data). These data indicated more extensive destruction of the Nb_6 with K^+ and formation of Nb-carbonate monomers, compared to the Rb^+ and Cs^+ analogues. The major differences between the solids obtained from CO_2-infused Rb/Cs^+-Nb_6 and K^+-Nb_6 solutions is evidenced in peaks b, d, and e. Peak b & e (more diminished for the K^+-analogue) are respectively the long μ_6-O-Nb_6 correlations and the Nb-Nb trans correlations. Diminution of these is consistent with more extensive deconstruction of the Nb_6-units. Second, the considerably larger peak d is consistent with the Nb-Nb correlations observed in the $[NbO(CO_3)_2]_2O$ dimer of **$Nb_{22}CO_3$**. Based on the CO_2 capture capacity and this PDF data, we presume the precipitate obtained from the CO_2-infused K^+-Nb_6 solution contains more extensive $[NbO(CO_3)_2O]_n$ networks and fewer intact Nb_6. The former is derived from CO_2-driven destruction of the latter, both by lowering the pH and coordinating reactive Nb-monomers. This is consistent with the SAXS data, where the CO_2-infused K^+-Nb_6 solution shows larger aggregates and more polydispersity, in addition to evidence for **$Nb_{22}CO_3$**. One might imagine, for example **$Nb_{22}CO_3$** units interconnected in a network of $[NbO(CO_3)_2O]_n$ chains. Prior SAXS studies of K, Rb and Cs Nb_6 solutions[35] indicated that Rb and Cs undergo contact ion-pairing with Nb_6, whereas K exhibits solvent-shared ion-pairing with Nb_6. This leads us to the hypothesis that direct ion-pairing of Rb-Nb_6

and Cs-Nb_6 provides stabilization and less exposure to CO_2/CO_3^{2-} at the air-water interface.

SFG spectroscopy provided insight into the direct role of niobyl in CO_2 capture, at the air-water interface. SFG is a highly interface-specific nonlinear optical technique, which is used for probing molecular ordering at buried surfaces and interfaces.[36] Earlier studies utilized SFG to study CO_2 capture at the air/liquid interface of amine-based carbon capture sorbents.[37-40] Richmond and co-workers observed noticeable changes in SFG spectra at the air/monoethanol amine interface upon reaction with CO_2, indicating presence of charged species and formation of carbamic acid upon the reaction with CO_2.[37-38] It was also evidenced by probing the -CH stretches of amino acids, that structural changes occurring at the interface during CO_2 absorption may block the subsequent capture events.[39] While these studies demonstrated the importance of interfacial reactions in CO_2 capture, they do not reported direct observation of carbonate species at the interface.

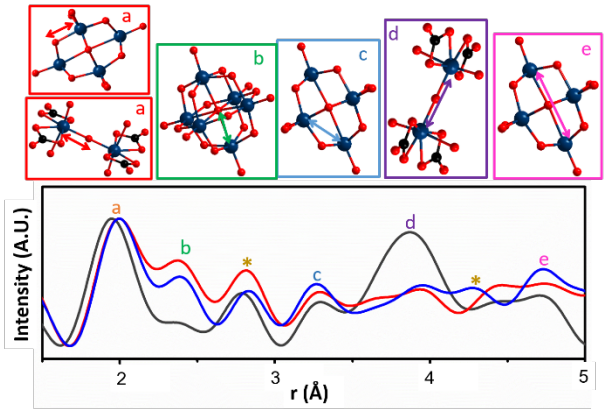

Figure 6. Normalized PDF (normalized to the peak labeled 'a') of alkali-Nb_6 solids after CO_2 exposure. K^+ (black), Rb^+ (red), and Cs^+ (blue) showing the Nb-O and Nb-Nb bond correlations. The peaks marked with asterisks (*) are due to alkali-O or alkali-Nb correlations, as determined from crystal structures.

Figure 7 shows the SFG spectra collected at the air/liquid interface of four different aqueous ~2 M hexaniobate (A-Nb_6) solutions before and after reaction with CO_2 (A=Cs, Rb, K, and TMA). These are the first direct observations of carbonate species during chemisorption at the air/liquid interface. The SFG spectra collected before exposure of the four different A-Nb_6 solutions to CO_2 show a very weak feature at 1412 cm^{-1} (**figure 7**, black curves), attributed to the symmetric stretch of the COO^- group;[41-42] indicative of carbonate formation at the interface under ambient CO_2 atmosphere, evidencing chemical reactivity of the hexaniobate solutions toward dilute atmospheric CO_2.

In an enriched CO_2 atmosphere (see SI for methods), the intensity of the carbonate feature increased significantly compared to the pristine Nb_6 solutions, suggesting increasing formation of carbonate at the interface for one and two days of exposure. The chemical reactivity of A-Nb_6 solutions toward CO_2 based on the 1412 cm^{-1} carbonate symmetric stretch peak intensity follows the order A = K > TMA > Cs > Rb (**figure 7**). Additionally, a vibrational feature observed for K-Nb_6 and Rb-Nb_6 solutions at 1650 cm^{-1} (water O-H stretch) became weaker after the reaction, indicating structural changes (transition or migration of formed interfacial carbonate species) after exposure to CO_2.

Bulk FTIR measurements of the solutions also reveal the formation of new carbonate species after exposure to CO_2, evident in the appearance of the carbonate symmetric stretch at 1047 cm^{-1} (**figure S9**) in addition to the red-shifting and increased intensities of the 1330 and 1590 cm^{-1} peaks (**figure S9**). In addition, the K, Rb, and Cs Nb_6 solutions show changes in the Nb=O, μ_2-ONb_2 and μ_6-ONb_6 vibrational peaks that are similar to those of the solids obtained from reactions (400 – 900 cm^{-1}, **figure S9)**. Specifically, pristine Nb_6 has a single μ_6-ONb_6 peak (515 cm^{-1}), a broad μ_2-ONb_2 band (620-650 cm^{-1}, variable with alkali), and a sharper Nb=O band (820 cm^{-1}). With CO_2 infusion, these bands all become split and extra peaks appear in this frequency range, representing different Nb-bonding environments including the $NbO_2(CO_3)_2$ pentagonal bipyramids found in $Nb_{22}CO_3$ and $Nb_{10}CO_3$. In fact, the IR of the CO_2-infused Rb-Nb_6 and Cs-Nb_6 solutions strongly resembles that of isolated $Nb_{22}CO_3$ crystals, again reinforcing this isolated phase is representative of the dominant solution speciation for these alkalis. Once again, the K-Nb_6 solution appears different with a shift of the μ_2-ONb_2 band to higher frequency (**figure S10**).

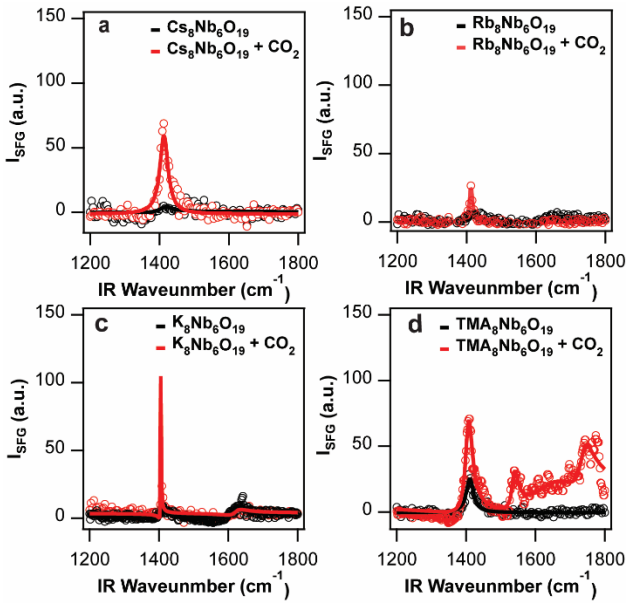

Figure 7. *ssp*-SFG spectra collected at the air/liquid interface of Cs-Nb_6 (**a**), Rb-Nb_6 (**b**), K-Nb_6 (c) and TMA-Nb_6 (d) between 1200 and 1800 cm^{-1}. SFG spectra (symbols) and fits (lines) are before (black) and after (red) exposure to a CO_2 atmosphere for one day.

Interestingly, the SFG spectrum of TMA hexaniobate solution after one and two days of reaction with CO_2 contains four carbonate spectral features (**figure 7d and figure S11**: 1408, 1540, 1664, and 1745 cm^{-1}. The 1408 and 1540 cm^{-1} peaks are assigned to the carbonate symmetric and asymmetric stretches, respectively; the 1664 cm^{-1} feature (**figure S11**) is due to the asymmetric stretch of bidentate bicarbonate (i.e. bound to Nb), and the 1760 cm^{-1} peak is attributed to the carbonate C=O stretch. However, the corresponding bulk FTIR spectrum shows less change in the carbonate stretching region, before and after CO_2 exposure (**figure S9**), despite the SFG signal showing considerable CO_3^- formation at the interface. Meanwhile, changes are observed in the Nb-O region, indicating evolution in Nb-POM speciation that differs from the three alkali-Nb_6 solutions. In this region, the μ_6-ONb_6 peak is split, the μ_2-ONb_2 band is shifted to higher frequency and broadened (2 or more overlapping peaks). This is consistent with the formation of the Nb_{24}-POM in the bulk solution,[25] also indicated by the Raman (**figure S12**) and SAXS, discussed below. Raman of the CO_2-infused TMA-Nb_6 (1M and 2M) shows the simple spectrum consistent with Nb_{24}. The SAXS (**figure 8a**) shows the typical scattering pattern of the Nb_{24}-POM ($H_xNb_{24}O_{72}$, x~9), first crystallized in 2006[43] and also observed prior by SAXS in several studies.[21, 25, 44-45] The PDDF analysis (**figure 8b**, **S13**, pair distance distribution function) is a

probability plot of scattering vectors obtained by a Fourier transform of the reciprocal space scattering data. The observed profile with the shoulder on the left typifies a core-shell geometry[46] such as that exhibited by Nb_{24}. **Figure S14** compares the scattering of the four studied A-Nb_6 solutions infused with CO_2, highlighting solution speciation differences between A=alkali and A=TMA.

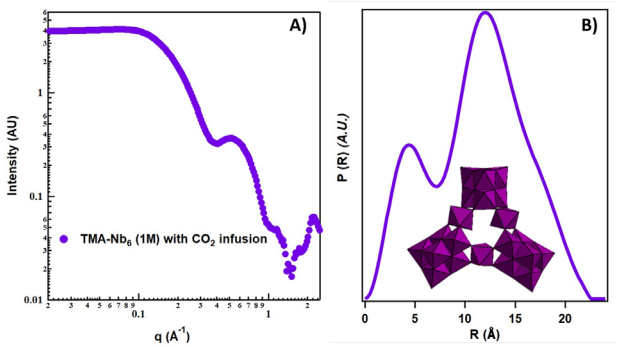

Figure 8. A) SAXS of CO_2-infused TMA-Nb_6, showing characteristic scattering of Nb_{24}. B) PDDF, typifying a core-shell type structure such as Nb_{24} (purple polyhedral representation, inset).

The SAXS data together with the SFG and bulk IR solution data suggest that TMA-Nb_6 solutions chemisorb considerable CO_2 directly at the interface via carbonate formation, but Nb-carbonate POMs are not stabilized and isolated without the presence of alkalis. Instead, Nb_{24} forms, in response to the pH decrease, as indicated by computational and experimental speciation studies.[24, 27] Nb_{24} does not have available metal sites to bind carbonate in a bidentate fashion, as is observed in the isolated POMs. Alternatively, the carbonate observed in the bulk could be either Nb-carbonate monomers that are not observable by SAXS, or free bicarbonate.

The impact of the newly formed interfacial species on the structure and ordering of interfacial water was also investigated by collecting SFG spectra over the O-H spectral region (3000-3800 cm^{-1}) (**figure S15**). The hydrogen-bonded OH oscillators consist of three broad peaks, 3100, 3200, and 3400 cm^{-1}, from strongly to weakly-hydrogen bonded water O-H groups. The non-hydrogen bonded water O-H groups vibrate at ~ 3700 cm^{-1}.[47-48] These SFG spectral features of the different A-Nb_6 solutions before reaction with CO_2 appear different from each other, highlighting the role of the identity of the counter cation and the ion-pairs that it forms with the Nb-species at the air/liquid interface. For instance, the weakly hydrogen-bonded 3400 cm^{-1} band disappeared at the air/Cs-Nb_6 (aq) interface and blue shifted to 3600 cm^{-1} at the air/Rb-Nb_6 (aq) interface. Also interesting is the disappearance of the free water O-H stretch at the air/TMA-Nb_6 (aq) interface (~ 3700 cm^{-1}), suggesting that the TMA counterion is relatively more surface active, due to its hydrophobic nature. Also, we observe the strongest before-exposure 1400 cm^{-1} carbonate peak with TMA. This may imply that TMA creates a favorable reaction environment at the interface even under ambient conditions.

Since these high concentration Nb_6-solutions are very alkaline due to protonation of their basic oxygens, we must also consider the reaction of free OH with CO_2:

$$CO_2\ (g) + OH^-\ (aq) \rightarrow HCO_3^-\ (aq) \qquad (2)$$

On the other hand, with $Nb_{22}CO_3$ as a predominant product, the stoichiometric reaction of the Rb-Nb_6 and Cs-Nb_6 solutions produce free hydroxide:

$$11[Nb_6O_{19}]^{8-} + 48CO_2\ (g) + 2H_2O \rightarrow 3[Nb_{22}O_{53}(CO_3)_{16}]^{28-} + 4OH^- \qquad (3)$$

The reaction stoichiometry also implies that Nb_6 alone can supply almost all the oxos required to react with CO_2 and produce **$Nb_{22}CO_3$**, plus the free hydroxide generated from the reaction can promote continued CO_2 chemisorption. If we consider the hypothetical end-product of this reaction in which all Nb is converted to coordination complexes with carbonate (i.e. $[NbO(CO_3)_2]_\infty$), the reaction stoichiometry can be written:

$$[Nb_6O_{19}]^{8-} + 12CO_2\ (g) + H_2O \rightarrow [NbO(CO_3)_2]_6^{6-} + 2OH^- \qquad (4)$$

Comparing equation (3) and (4); the key ratio of hydroxide produced per CO_2 absorbed is $4.4CO_2$:0.36OH for the former and $2CO_2$:0.3OH for the latter. This means that more extensive fragmentation of the Nb_6 (i.e. equation 4) leads to higher production of free hydroxide per CO_2 molecule absorbed. The higher CO_2 capacity of the K-Nb_6 solutions is demonstrated by multiple lines of evidence throughout this study. Considering that CO_2 chemisorption typically decreases solution pH (i.e. equation 1), the tandem CO_2 chemisorption plus OH^- formation (equations 3 & 4) of the Nb_6 solutions is encouraging, and highlights yet another role of basic metal oxoclusters and oxoanions in CO_2 capture.

Finally, we performed SFG measurements in the carbonate and OH regions at the air/100mM (**figure S16**) and 6M (**figure S17**) aqueous KOH interface before and after exposure to CO_2. The 100 mM KOH solution provided a pH comparable to that of the studied Nb-POM solutions, while the 6M KOH solution provided potassium concentration closer to that of the Nb-POM solutions. These control studies were also executed with 6M TMAOH (**figures S19-S20**), and all control studies showed similar results. For all solutions, interfacial CO_3^{2-} peaks that were observed in the Nb-POM solutions (**figure 7**) are absent in the CO_2-exposed hydroxide solutions (**figures S16b, S17b, S19b**), indicating the surface carbonate is Nb-bound.

The SFG spectra in the OH regions are similar between the hydroxide and Nb_6 solutions. The KOH solutions exhibit same prior-discussed broad bands at 3200 and 3400 cm^{-1}, and a sharper peak at ~ 3700 cm^{-1}; respectively H-bonded water and water with one O-H oriented in the gas phase, without H-bonding.[36, 47] These peaks are more intense for the lower concentration KOH, due to the smaller population of ions at the interface. After exposure to CO_2, minimal spectral differences were observed, consistent with minimal change in the water spectral region. Similar to the TMA-Nb_6 solution, the TMAOH does not exhibit the sharp 3700 cm^{-1} feature, and there is more suppression of the broader features upon CO_2 exposure indicating higher ion concentration at these relatively hydrophobic interfaces. Carbonate is observed in the bulk solutions, **figure S18** and **S20**, but less so for the TMAOH solutions.

In summary, this study has provided atomic-level detail of the reaction of aqueous Nb_6-polyoxometalates with gaseous CO_2, leading to tandem Nb-POM speciation change and CO_2 chemisorption via formation of Nb-carbonate complexes. SCXRD of Nb-carbonate POMs provided models to understand reaction pathways probed by bulk solution (SAXS, FTIR, Raman) and air-water interfacial (SFG) characterization. This study provides the first example, to our knowledge, where gas is used to invoke changes in POM-speciation, which is typically executed with addition of dissolved acid or base. The role of the countercations remains less-well understood. Solutions with K^+-counterions chemisorbed substantially more CO_2 than those with Rb^+ or Cs^+, and we attribute this to the nature of ion-association with the Nb-POM species, at both the interface and in bulk. TMA^+ counterions readily support formation of Nb-carbonate species at the interface, but do not necessarily stabilize them in bulk POM solutions, noted by multiple lines of evidence. Future studies include understanding more specifically the synergistic role of alkalis and high oxidation state metal oxoanions in carbon capture reactions, both direct air capture and in enhanced CO_2 environments, as solids and solutions.

ASSOCIATED CONTENT

Supporting Information. A PDF document containing experimental methods and supplementary spectra and data tables of the various analyses presented in this paper. Crystallographic information files (cif) for Rb-$Nb_{10}CO_3$ and Cs-$Nb_{10}CO_3$, Rb-$Nb_{22}CO_3$, (also deposited in the Cambridge Crystallographic Data Center, CCDC, with code numbers 2350564-2350566). This material is available free of charge via the Internet at http://pubs.acs.org.

AUTHOR INFORMATION

Corresponding Author

* may.nyman@oregonstate.edu
*auysal@anl.gov

Author Contributions

The manuscript was written through contributions of all authors.

ACKNOWLEDGMENT

This work was supported by the U.S. Department of Energy, Basic Energy Sciences, grant DE-SC0022278. Part of this work was conducted at ANL (SFG studies), operated by UChicago Argonne, LLC for the United States Department of Energy (U.S. DOE).

ABBREVIATIONS

SFG, sum frequency generation; SAXS, small-angle X-ray scattering, PDF, pair distribution function; DAC (direct air capture).

REFERENCES

1. Gao, W. L.; Liang, S. Y.; Wang, R. J.; Jiang, Q.; Zhang, Y.; Zheng, Q. W.; Xie, B. Q.; Toe, C. Y.; Zhu, X. C.; Wang, J. Y.; Huang, L.; Gao, Y. S.; Wang, Z.; Jo, C.; Wang, Q.; Wang, L. D.; Liu, Y. F.; Louis, B.; Scott, J.; Roger, A. C.; Amal, R.; Heh, H.; Park, S. E., Industrial carbon dioxide capture and utilization: state of the art and future challenges. *Chem Soc Rev* **2020,** *49* (23), 8584-8686.
2. Tao, Z. Y.; Tian, Y. M.; Ou, S. Y.; Gu, Q. F.; Shang, J., Direct air capture of CO_2 by metal cation-exchanged LTA zeolites: Effect of the charge-to-size ratio of cations. *Aiche J* **2023,** *69* (8).
3. Morrison, J.; Jauffret, G.; Galvez-Martos, J. L.; Glasser, F. P., Magnesium-based cements for CO_2 capture and utilisation. *Cement Concrete Res* **2016,** *85*, 183-191.
4. Rausis, K.; Stubbs, A. R.; Power, I. M.; Paulo, C., Rates of atmospheric CO_2 capture using magnesium oxide powder. *Int J Greenh Gas Con* **2022,** *119*.
5. de Jonge, M. M. J.; Daemen, J.; Loriaux, J. M.; Steinmann, Z. J. N.; Huijbregts, M. A. J., Life cycle carbon efficiency of Direct Air Capture systems with strong hydroxide sorbents. *Int J Greenh Gas Con* **2019,** *80*, 25-31.
6. Zolfaghari, Z.; Aslani, A.; Zahedi, R.; Kazzazi, S., Simulation of carbon dioxide direct air capture plant using potassium hydroxide aqueous Solution: Energy optimization and CO_2 purity enhancement. *Energ Convers Man-X* **2024,** *21*.
7. Rim, G.; Priyadarshini, P.; Song, M. Y.; Wang, Y. X.; Bai, A. D.; Realff, M. J.; Lively, R. P.; Jones, C. W., Support Pore Structure and Composition Strongly Influence the Direct Air Capture of CO_2 on Supported Amines. *J Am Chem Soc* **2023,** *145* (13), 7190-7204.
8. Reddy, M. K. R.; Xu, Z. P.; Lu, G. Q.; da Costa, J. C. D., Layered double hydroxides for CO_2 capture: Structure evolution and regeneration. *Ind Eng Chem Res* **2006,** *45* (22), 7504-7509.
9. Zheng, S. X.; Song, C. H.; Curria, M. C.; Ren, Z. J.; White, C. E., Ca-Based Layered Double Hydroxides for Environmentally Sustainable Carbon Capture. *Environ Sci Technol* **2023,** *57* (45), 17212-17224.
10. Veerabhadrappa, M. G.; Maroto-Valer, M. M.; Chen, Y. H.; Garcia, S., Layered Double Hydroxides-Based Mixed Metal Oxides: Development of Novel Structured Sorbents for CO_2 Capture Applications. *Acs Appl Mater Inter* **2021,** *13* (10), 11805-11813.
11. Chouikhi, N.; Cecilia, J. A.; Vilarrasa-García, E.; Besghaier, S.; Chlendi, M.; Duro, F. I. F.; Castellon, E. R.; Bagane, M., CO_2 Adsorption of Materials Synthesized from Clay Minerals: A Review. *Minerals-Basel* **2019,** *9* (9), 514.
12. Grayevsky, R.; Reiss, A. G.; Emmanuel, S., Carbon Storage through Rapid Conversion of Forsterite into Solid Oxalate Phases. *Energ Fuel* **2023,** *37* (1), 509-517.
13. Socolow, R.; Desmond, M.; Aines, R.; Blackstock, J.; Bolland, O.; Kaarsberg, T.; Lewis, N.; Mazzotti, M.; Pfeffer, A.; Sawyer, K.; Siirola, J.; Smit, B.; Wilcox, J. *Direct Air Capture of CO_2 with Chemicals, A Technology Assessment for the APS Panel on Public Affairs*; 2011.
14. Bhatti, U. H.; Shah, A. K.; Kim, J. N.; You, J. K.; Choi, S. H.; Lim, D. H.; Nam, S.; Park, Y. H.; Baek, I. H., Effects of Transition Metal Oxide Catalysts on MEA Solvent Regeneration for the Post-Combustion Carbon Capture Process. *Acs Sustain Chem Eng* **2017,** *5* (7), 5862-5868.
15. Lai, Q. H.; Toan, S.; Assiri, M. A.; Cheng, H. G.; Russell, A. G.; Adidharma, H.; Radosz, M.; Fan, M. H., Catalyst-$TiO(OH)_2$ could drastically reduce the energy consumption of CO_2 capture. *Nat Commun* **2018,** *9*, 2672.
16. Gao, H. X.; Huang, Y. F.; Zhang, X. W.; Bairq, Z. A. S.; Huang, Y. Q.; Tontiwachwuthikul, P.; Liang, Z. W., Catalytic performance and mechanism of SO_4^{2-}/ZrO_2/SBA-15 catalyst for CO_2 desorption in CO_2-loaded monoethanolamine solution. *Appl Energ* **2020,** *259*, 114179.
17. Phan, D. T.; Maeder, M.; Burns, R. C.; Puxty, G., Catalysis of CO_2 absorption in aqueous solution by vanadate and sulfate and their application to post combustion capture. *Int J Greenh Gas Con* **2015,** *36*, 60-65.
18. Ribó, E. G.; Mao, Z. W.; Hirschi, J. S.; Linsday, T.; Bach, K.; Walter, E. D.; Simons, C. R.; Zuehlsdorff, T. J.; Nyman, M., Implementing vanadium peroxides as direct air carbon capture materials. *Chem Sci* **2023**.
19. Black, J. R.; Nyman, M.; Casey, W. H., Rates of Oxygen Exchange between the $[H_xNb_6O_{19}]^{8-x}$ (aq) Lindqvist Ion and Aqueous Solutions. *J Am Chem Soc* **2006,** *128* (45), 14712–14720.
20. Nyman, M.; Alam, T. M.; Bonhomme, F.; Rodriguez, M. A.; Frazer, C. S.; Welk, M. E., Solid-state structures and solution behavior of alkali salts of the $[Nb_6O_{19}]^{8-}$ Lindqvist ion. *J Clust Sci* **2006,** *17* (2), 197-219.
21. Amiri, M.; Martin, N. P.; Feng, C. L.; Lovio, J. K.; Nyman, M., Deliberate Construction of Polyoxoniobates Exploiting the Carbonate Ligand. *Angew Chem Int Edit* **2021,** *60* (22), 12461-12466.
22. Wu, Y. L.; Li, X. X.; Qi, Y. J.; Yu, H.; Jin, L.; Zheng, S. T., {NbO(OH)(CO)}: A Macromolecular Polyoxometalate with Close to 300 Niobium Atoms. *Angew Chem Int Edit* **2018,** *57* (28), 8572-8576.
23. Tsunashima, R.; Long, D. L.; Miras, H. N.; Gabb, D.; Pradeep, C. P.; Cronin, L., The Construction of High-Nuclearity Isopolyoxoniobates with Pentagonal Building Blocks: $[HNb_{27}O_{76}]^{16-}$ and $[H10Nb_{31}O_{93}(CO_3)]^{23-}$. *Angew Chem Int Edit* **2010,** *49* (1), 113-116.
24. Petrus, E.; Segado-Centellas, M.; Bo, C. R., Computational Prediction of Speciation Diagrams and Nucleation Mechanisms: Molecular Vanadium, Niobium, and Tantalum

Oxide Nanoclusters in Solution. *Inorg Chem* **2022,** *61* (35), 13708-13718.
25. Sures, D.; Segado, M.; Bo, C.; Nyman, M., Alkali-Driven Disassembly and Reassembly of Molecular Niobium Oxide in Water. *J Am Chem Soc* **2018,** *140* (34), 10803-10813.
26. Martin, N. P.; Petrus, E.; Segado, M.; Arteaga, A.; Zakharov, L. N.; Bo, C.; Nyman, M., Strategic Capture of the {Nb_7} Polyoxometalate. *Chem-Eur J* **2019,** *25* (45), 10580-10584.
27. Nyman, M.; Rahman, T.; Colliard, I., Decaniobate: The Fruit Fly of Niobium Polyoxometalate Chemistry. *Acc. Chem. Res.* **2023,** *56* (24), 3616–3625.
28. Zhang, D. Q.; Qin, Z. C.; Yang, X. Y.; Zhu, H. B.; Cao, M. S., Study on synthesis and evolution of sodium potassium niobate ceramic powders by an oxalic acid-based sol-gel method. *J Sol-Gel Sci Techn* **2011,** *57* (1), 31-35.
29. Jehng, J. M.; Wachs, I. E., Niobium Oxide Solution Chemistry. *J Raman Spectrosc* **1991,** *22* (2), 83-89.
30. Deblonde, G. J. P.; Chagnes, A.; Weigel, V.; Cote, G., Direct precipitation of niobium and tantalum from alkaline solutions using calcium-bearing reagents. *Hydrometallurgy* **2016,** *165*, 345-350.
31. Hardcastle, F. D.; Wachs, I. E., Determination of Niobium Oxygen Bond Distances and Bond Orders by Raman-Spectroscopy. *Solid State Ionics* **1991,** *45* (3-4), 201-213.
32. Ribó, E. G.; Mao, Z. W.; Hirschi, J. S.; Linsday, T.; Bach, K.; Walter, E. D.; Simons, C. R.; Zuehlsdorff, T. J.; Nyman, M., Implementing vanadium peroxides as direct air carbon capture materials. *Chem Sci* **2024,** *15* (5), 1700-1713.
33. Potton, J. A.; Daniell, G. J.; Rainford, B. D., Particle-Size Distributions from Sans Data Using the Maximum-Entropy Method. *J Appl Crystallogr* **1988,** *21*, 663-668.
34. Ilavsky, J.; Jemian, P. R., : tool suite for modeling and analysis of small-angle scattering. *J Appl Crystallogr* **2009,** *42*, 347-353.
35. Antonio, M. R.; Nyman, M.; Anderson, T. M., Direct Observation of Contact Ion-Pair Formation in Aqueous Solution. *Angew Chem Int Edit* **2009,** *48* (33), 6136-6140.
36. Bonn, M.; Nagata, Y.; Backus, E. H. G., Molecular Structure and Dynamics of Water at the Water-Air Interface Studied with Surface-Specific Vibrational Spectroscopy. *Angew Chem Int Edit* **2015,** *54* (19), 5560-5576.
37. McWilliams, L. E.; Valley, N. A.; Wren, S. N.; Richmond, G. L., A means to an interface: investigating monoethanolamine behavior at an aqueous surface. *Phys Chem Chem Phys* **2015,** *17* (33), 21458-21469.
38. McWilliams, L. E.; Valley, N. A.; Vincent, N. M.; Richmond, G. L., Interfacial Insights into a Carbon Capture System: CO_2 Uptake to an Aqueous Monoethanolamine Surface. *J Phys Chem A* **2017,** *121* (41), 7956-7967.
39. Premadasa, U. I.; Dong, D. P.; Stamberga, D.; Custelcean, R.; Roy, S.; Ma, Y. Z.; Bocharova, V.; Bryantsev, V. S.; Doughty, B., Chemical Feedback in the Self-Assembly and Function of Air-Liquid Interfaces: Insight into the Bottlenecks of CO2 Direct Air Capture. *ACS Appl Mater Inter* **2023,** *15* (15), 19634-19645.
40. Premadasa, U. I.; Kumar, N.; Zhu, Z.; Stamberga, D.; Li, T.; Roy, S.; Carrillo, J.-M. Y.; Einkauf, J. D.; Custelcean, R.; Ma, Y.-Z.; Bocharova, V.; Bryantsev, V. S.; Doughty, B., Synergistic Assembly of Charged Oligomers and Amino Acids at the Air–Water Interface: An Avenue toward Surface-Directed CO_2 Capture. *ACS Appl. Mater. Interfaces* **2024,** *16* (9), 12052–12061.
41. Musegades, L. J.; Curtin, O. P.; Cyran, J. D., Determining the Surface pKa of Perfluorooctanoic Acid. *The Journal of Physical Chemistry C* **2024,** *128* (5), 1946-1951.
42. Sthoer, A.; Adams, E. M.; Sengupta, S.; Corkery, R. W.; Allen, H. C.; Tyrode, E. C., La3+ and Y3+ interactions with the carboxylic acid moiety at the liquid/vapor interface: Identification of binding complexes, charge reversal, and detection limits. *J Colloid Interf Sci* **2022,** *608*, 2169-2180.
43. Bontchev, R. P.; Nyman, M., Evolution of polyoxoniobate cluster anions. *Angew Chem Int Edit* **2006,** *45* (40), 6670-6672.
44. Rahman, T.; Martin, N. P.; Jenkins, J. K.; Elzein, R.; Fast, D. B.; Addou, R.; Herman, G. S.; Nyman, M., Nb2O5, LiNbO3, and (Na, K)NbO3 Thin Films from High-Concentration Aqueous Nb-Polyoxometalates. *Inorg Chem* **2022,** *61* (8), 3586-3597.
45. Rahman, T.; Petrus, E.; Segado, M.; Martin, N. P.; Palys, L. N.; Rambaran, M. A.; Ohlin, C. A.; Bo, C.; Nyman, M., Predicting the Solubility of Inorganic Ions Pairs in Water. *Angew Chem Int Edit* **2022,** *61* (19).
46. Putnam, C. D.; Hammel, M.; Hura, G. L.; Tainer, J. A., X-ray solution scattering (SAXS) combined with crystallography and computation: defining accurate macromolecular structures, conformations and assemblies in solution. *Q Rev Biophys* **2007,** *40* (3), 191-285.
47. Fan, Y. B.; Chen, X.; Yang, L. J.; Cremer, P. S.; Gao, Y. Q., On the Structure of Water at the Aqueous/Air Interface. *J Phys Chem B* **2009,** *113* (34), 11672-11679.
48. Litman, Y.; Chiang, K. Y.; Seki, T.; Nagata, Y.; Bonn, M., Surface stratification determines the interfacial water structure of simple electrolyte solutions. *Nat Chem* **2024**.

For Table of Contents only